Fall August 7, 2017

Fully-Packaged Carbon Nanotube Supercapacitors by Direct Ink Writing on Flexible Substrates

Bolin Chen, *Iowa State University*
Yizhou Jiang, *University of Illinois Chicago*
Xiaohui Tang, *Iowa State University*
Yayue Pan, *University of Illinois at Chicago*
Shan Hu, *Iowa State University*

Fully-Packaged Carbon Nanotube Supercapacitors by Direct Ink Writing on Flexible Substrates

Bolin Chen[1], Yizhou Jiang[2], Xiaohui Tang[1], and Yayue Pan[2,], Shan Hu[1,*]*

[1]Department of Mechanical Engineering, Iowa State University, IA, 50011, USA

[2]Department of Mechanical and Industrial Engineering, University of Illinois Chicago, IL, 60607, USA

*Corresponding authors: Shan Hu (shanhu@iastate.edu), Yayue Pan (yayuepan@uic.edu)

KEYWORDS

Direct Ink Writing, Supercapacitor, Carbon nanotube, 3D printing, Flexible electronics

ABSTRACT

The ability to print fully-packaged integrated energy storage components (e.g. supercapacitors) is of critical importance for the practical application of printed electronics. Due to the limited variety of printable materials, most studies on printed supercapacitors focus on printing the electrode materials but rarely the full-packaged cell. Herein, this work presented for the first time, the printing of a fully-packaged single-wall carbon nanotube based supercapacitors with direct ink writing (DIW) technology. Enabled by the developed ink formula, DIW setup, and cell architecture, the whole printing process is mask-free, transfer-free, and alignment-free with

precise and repeatable control on the spatial distribution of all constituent materials. Studies on cell design shows that wider electrode pattern and narrower gap distance between electrodes lead to higher specific capacitance. The as-printed fully-packaged supercapacitors have energy and power performances that are among the best in recently reported planar carbon-based supercapacitors that are only partially-printed or non-printed.

1. Introduction

Printed electronics offer the promise of low cost, rapid prototyping, easy customization, and even flexible and conformal devices when printed on soft substrates. Printed electronic components have been extensively studied, such as transistors[1,2], sensors[3], displays[4], etc. Since power supply is an indispensable component of any electronics, to fully realize the promise of printed electronics, printed power sources have to be developed. Recently, supercapacitors have emerged as a promising energy storage device, due to its high power, long cycle life, and its ability to bridge the energy and power gap between batteries and conventional dielectric capacitors. Supercapacitors are widely used in electronic systems where fast and frequent charging/discharging is required. Hybrid power sources integrating batteries and supercapacitors together provide both high energy and high power at the same time.

A fully-packaged supercapacitor consists of integrated functional parts and structural parts. Functional parts are components that contribute directly to the energy storage, including electrode, electrolyte, and separator. While structural parts are those that do not store energy but are necessary for achieving stable performances, including sealed casing, support substrates, etc. Since each component is made of very different materials, printing a fully-packaged supercapacitor is challenging but necessary for practical application of printed supercapacitors.

Additive Manufacturing (AM), also known as 3D Printing or Direct Digital Manufacturing, is a class of technologies that fabricate a three-dimensional physical model directly from its digital design, by accumulating materials, usually in a layer-by-layer way. Considering the unique strengths such as maskless, one-step operation, and little material waste, AM technologies such as Fused Deposition Modeling (FDM), Inkjet Printing, and Direct Ink Writing (DIW) have been widely investigated for printed electronics in the past decade [5–14]. The major drawback of inkjet printing is the limited variety of printable materials: materials need to have both flowability and jettability, which means only low-viscosity materials can be processed in this technique. The major disadvantage of FDM is that its printing resolution is low, usually in the range of 50~200 μm. In addition, the feedstocks have to be filaments that can be melted in a low temperature (<200 ^{o}C). Compared with the Inkjet Printing and FDM technologies, the DIW technology has much wider choice of feedstocks ranging from highly viscous polymer gels to highly shear thinning colloidal suspensions, which allows an unrivaled freedom for choosing and preparing proper inks for the multi-material supercapacitor design. DIW method has demonstrated the capability of producing highly accurate, repeatable, and complex microstructures of any shape from a wide choice of materials in room temperatures, directly from digital design without the use of any masters or masks[15–18].

So far, most studies on printed supercapacitors focus on printing the electrode materials but rarely the fully-packaged cell. The printed electrodes are later assembled with other non-printed components. For example, Xie et al. used laser to pattern graphene/nickel electrodes on poly(ethylene terephthalate) (PET) film and later manually casted polyvinyl alcohol/lithium chloride gel electrolyte onto the electrodes and sealed the cell with PET by hot-melt glue[19]. Wang et al. used a commercial inkjet printer to pattern multi-wall carbon nanotube based

nanocomposite electrodes on paper and later sandwiched the two electrodes with an electrolyte-soaked separator in between. Finally, they used adhesive tape to seal the cell[20]. Tehrani et al. used a screen presser and a series of masks to print carbon-silver electrodes, gel electrolyte, adhesives, and finally assembled two electrolyte loaded electrodes into a sealed cell with adhesives[21]. Although excellent electrochemical performances have been reported from these studies, the printing/patterning techniques used in these studies (laser processing, ink-jet printing, screen-printing) involve multiple aligning, transferring, and assembling steps to finally produce a fully-packaged supercapacitor. These intermediate steps add uncertainties to the volume, mass, and performances of the as-made supercapacitors and decrease repeatability, which is very important for practical manufacturing.

Herein, we report for the first time the use of DIW technology for printing fully-packaged flexible supercapacitors. All components of the supercapacitor are directly written on a flexible polyimide substrate, including single-wall carbon nanotube (SW-CNT) electrode, polyvinyl alcohol (PVA) based gel electrolyte, and silicone for cell packaging and sealing. Single-wall carbon nanotube (SW-CNT) is used as the model electrode material in this study because it has high electrical conductivity, mechanical strength, as well as high specific surface area that is open to surface functionalization for enhanced energy storage performance. PVA can form flexible and quasi-solid-state electrolyte when mixed with a variety of aqueous electrolyte solution, such as sulfuric acid (H_2SO_4), phosphoric acid (H_3PO_4), lithium chloride (LiCl), potassium hydroxide, etc. Here, PVA-LiCl system is chosen as the model electrolyte for its neutral and benign nature. The entire printing process is assembly-free, transfer-free, and mask-free. DIW controls the spatial distribution of printed materials with high accuracy and

repeatability, which is demonstrated by the printing of multiple highly symmetric supercapacitor connected in series.

2. Experimental Section

2.1 Preparation of Carbon Nanotube Ink and Polymer Gel Electrolyte Ink

High purity and large surface area SW-CNT (purity >95%, specific surface area >1075 $m^2 g^{-1}$) is purchased from Timesnano (product code: TNSAR, Chengdu, China) and used as received. 32mg SW-CNT and 120 mg sodium n-dodecyl sulfate surfactant (SDS, Sigma Aldrich, USA) are added into 40 ml deionized (DI) water, and stirred at 300 rpm using magnetic stirring bar for 5 minutes. The mixture is then placed inside an ice-water bath and subjected to 10 minutes of probe sonication (QSonica Q500, 50% power) to disperse SW-CNT uniformly in the DI water. To prepare PVA-based gel electrolyte, 6g of PVA powder (Mowiol® 18-88, Sigma Aldrich, USA) and 12g of lithium chloride powder (>99.0%, Sigma Aldrich, USA) are added to 40 ml of DI water and stirred on a 85°C hot plate until the mixture became a clear and glue-like gel. Silicone rubber is purchased from Nanda 705 RTV Silicon Rubber (Liyang, China) and used as received.

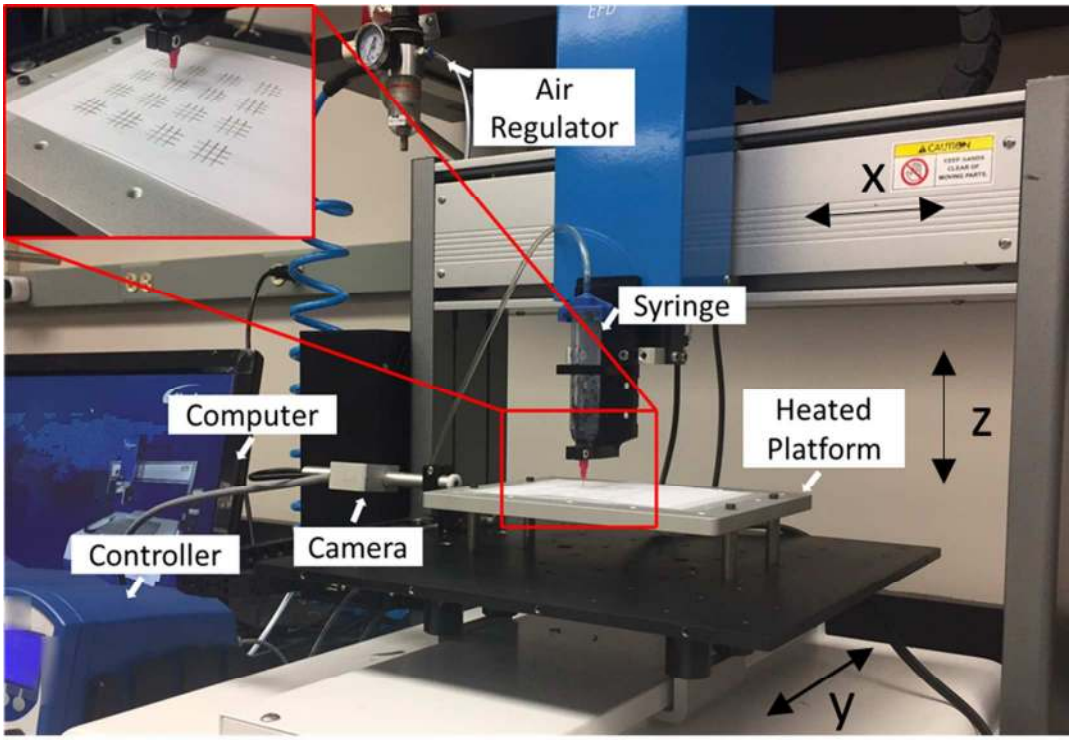

Figure 1. Photograph of the developed direct writing testbed.

2.2 Direct ink writing setup

In this study, a DIW testbed is developed to fabricate the fully-packaged supercapacitor, including electrode, electrolyte, and sealed package. DIW is achieved by dispensing inks through syringe needles in close proximity to a moving platform in a layer-by-layer way. As shown in Figure. 1, the testbed is equipped with a syringe needle, an air-pressure controller to regulate ink dispensing rate, a heated platform, a charge coupled device (CCD) camera, an X-Z stage, and a Y stage. The syringe needle is mounted on an X-Z stage, and the platform is placed on a Y stage. The CCD camera is used to monitor the ink dispensing in real time and to measure the distance between tip and platform. The platform temperature is controlled and can be varied between 15 ~ 250 ^{o}C.

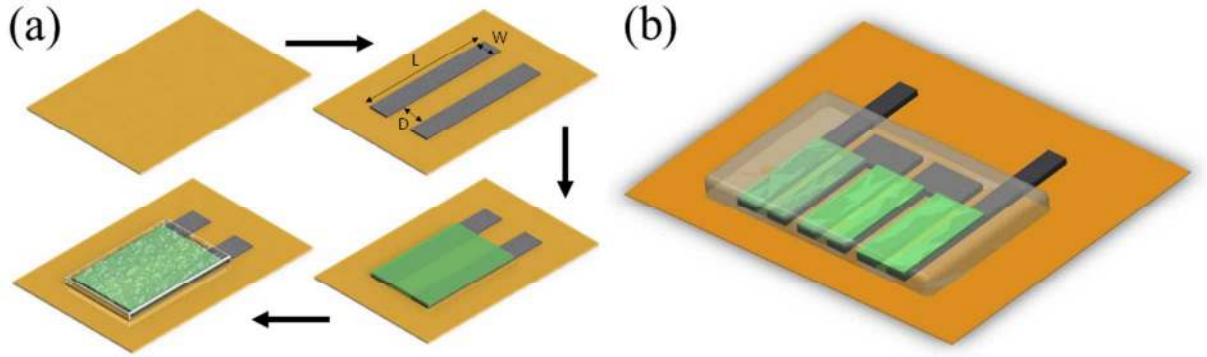

Scheme 1. (a) Schematic of layer design and printing process for DIW of the proposed supercapacitors. (b) An array of 3 identical cells connected in series

2.4 DIW of SW-CNT supercapacitor

The DIW process for rapid production of the proposed supercapacitor consists of four steps as illustrated in Scheme 1(a). During the entire printing process, the Kapton polyimide substrate (McMaster-Carr, USA) is fixed on the platform, which is controlled by the Y-stage. Firstly, 2ml SW-CNT ink is printed onto the Kapton substrate with a needle tip of 0.20mm inner diameter using 1.0 psi dispensing air pressure and 200mm/s writing speed (black region in Scheme 1(a)). With a platform temperature of 100 ^{o}C, the CNT solution is fully dried within 5 minutes. To remove surfactant and improve conductivity of the CNT electrode, the printed part is soaked in concentrated nitric acid for 20 minutes, quenched in DI water, and dried in air. Secondly, the dispensing tip moves up by 0.1 mm in the Z-direction to print the second layer. In the second layer, PVA electrolyte is then printed in the light green region in Scheme 1(a). To print the PVA layer, a needle tip with 0.41 mm inner diameter is placed above the Kapton substrate with a 0.4 mm gap distance (also known as the standoff distance). The pumping pressure is set at 25 psi and the substrate speed is set at 5 mm/s in the Y-direction. Finally, a layer of silicone rubber is printed in the transparent region in Scheme 1(a). The needle tip (0.84 mm inner diameter) is placed above the Kapton film substrate with a ~0.6 mm standoff distance. A pumping pressure of

30 psi and a platform moving speed of 10 mm/s are used to print the silicone rubber layer. The silicone rubber layer covers the whole supercapacitor leaving only two SW-CNT electrode legs exposed for electrical connection.

To study how the electrode and electrolyte pattern design affect the overall performance of the supercapacitor, single-cell supercapacitor designs with different geometry are printed following the procedure given in Scheme 1(a). Specifically, the width of the electrode ("W" in Scheme 1(a)) and different distance between electrodes ("D" in Scheme 1(a)) are varied and their effects on the supercapacitor performances are compared. Multi-cell supercapacitor design is also printed. The design shown in Scheme 1(b) is an array of three identical supercapacitors connected in series.

2.5 Material and Electrochemical Characterization

The viscosity of the CNT ink, PVA electrolyte ink, and silicon rubber ink are measured by Malvern Kinexus ultra+ rheometer at 25 °C, with shear rate ranging from 1 to 100 s^{-1}. Microscopic image of the as-printed SW-CNT electrode is taken from FEI Quanta 250 FEG Scanning Electron Microscope (SEM) at an operating voltage of 10 kV. The XPS measurements of surface composition of the electrodes are performed using a Kratos Amicus/ESCA 3400 instrument. The sample is irradiated with 240 W unmonochromated Mg Kα x-rays, and photoelectrons emit at 0° from the surface normal are energy analyzed using a DuPont type analyzer. The pass energy is set at 150 eV and either a Shirley or linear baseline is removed from all reported spectra. CasaXPS is used to process raw data files.

Galvanostatic charge-discharge (GCD), cyclic voltammetry (CV) and electrochemical impedance spectroscopy (EIS) are performed on the printed supercapacitors with Gamry

Reference 3000 electrochemical station. The capacitances of each device at different current densities are calculated from the discharge curves obtained from GCD tests using the formula

$$C = I/\frac{\Delta U}{\Delta t} \quad (1)$$

Where I is the applied discharge current (amp), Δt is discharge time (second), ΔU (volt) is the discharge voltage after IR drop is removed.

The gravimetric, areal and volumetric specific capacitances of each device at different current densities are calculated from the discharge curves obtained from GCD tests using the following equations

$$C_{sp,g} = \frac{C}{m} \quad (2)$$

$$C_{sp,areal} = \frac{C}{A} \quad (3)$$

$$C_{sp,vol} = \frac{C}{V} \quad (4)$$

Where m (g), A (cm^2) and V (cm^3) are the mass, area and volume of the active materials of all electrodes. Here, active materials are the printed CNTs (dark grey region in Scheme 1) that overlap with the electrolyte (green region in Scheme 1).

As pointed out by Gogotsi and Simon et al., volumetric energy density and power density can provide more reliable performance metrics for porous nanomaterial based thin film devices compared to gravimetric capacitance.[22] As a result, the volumetric energy density (Wh cm^{-3}) of each device is calculated using

$$E = \frac{0.5 \times C \times \Delta U^2}{3600 \times V} \quad (5)$$

The volumetric power density (W cm^{-3}) of the device is calculated from

$$P = \frac{E}{\Delta t} \times 3600 \quad (6)$$

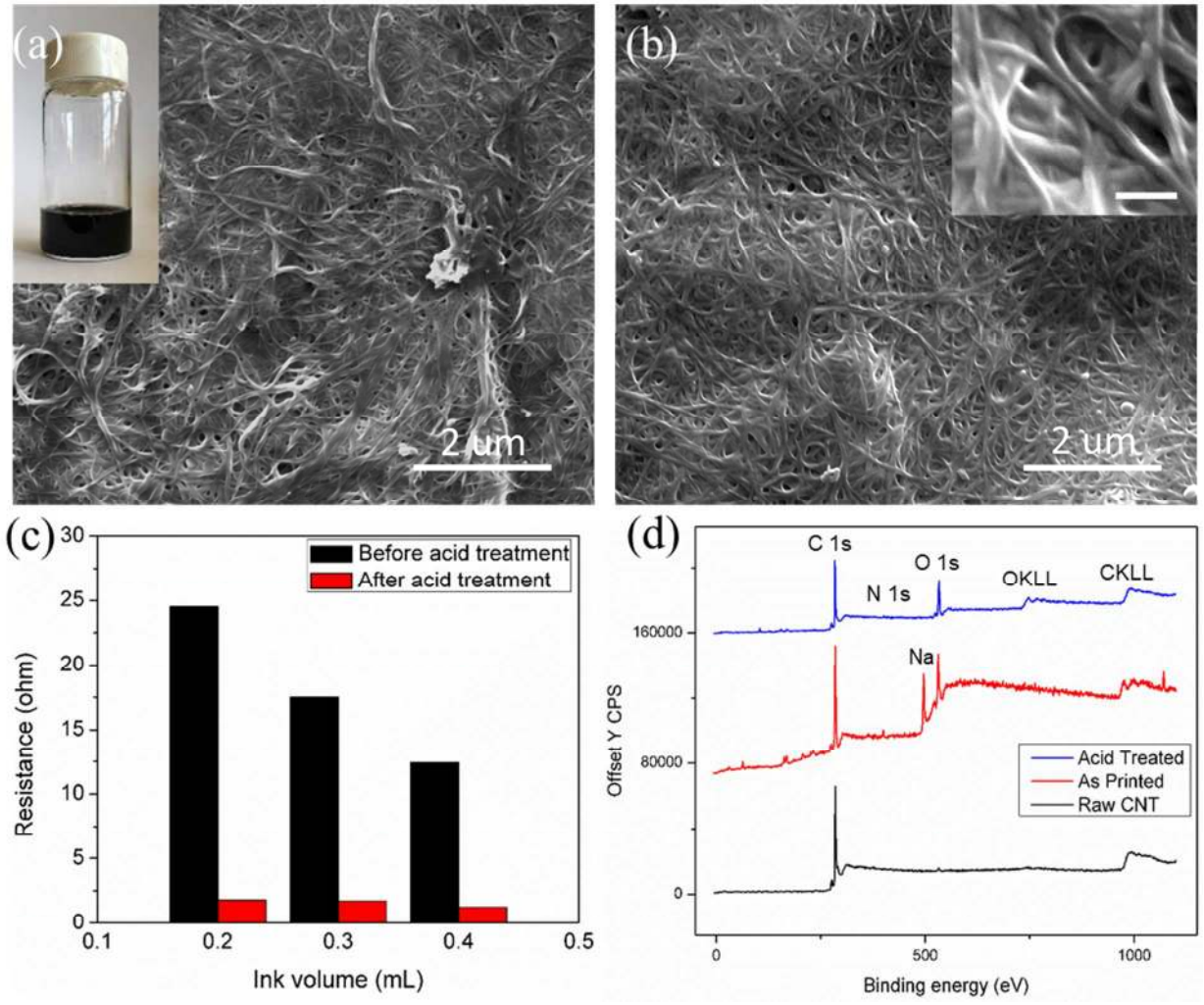

Figure 2. (a) SEM of as printed CNT electrode surface without acid-treatment; the inserted optical image shows the developed SW-CNT ink. (b) SEM of acid treated electrode surface with inserted high magnification image (scale bar 200 nm). (c) Change of resistance of printed traces with ink volume used before and after nitric acid treatment; (d) Full XPS spectrum of raw SW-CNT, as-printed SW-CNT without acid treatment, and with acid treatment.

3. Results and Discussion

The viscosity measurements of the inks for the SW-CNT electrode, PVA electrolyte, and silicone sealed package are plotted in Figure S1. The morphology of printed SW-CNT electrode before and after acid treatment are shown in Figure 2a-b. In as-printed electrodes, a layer of

surfactant on top of the SW-CNT can be seen in Figure 2a. After acid treatment, the surfactant top layer seems to be removed and the highly porous structure of the SW-CNT can be clearly seen in Figure 2b. The inserted image in Figure 2a shows the prepared SW-CNT ink. Figure S2 shows the cross-section SEM of SW-CNT electrode with an average thickness of 1.26 μm. Different volumes of SW-CNT ink (0.2, 0.3, and 0.4 ml) are used to print traces 10 mm long and 3 mm wide. Resistances of traces with and without nitric acid treatment are measured and compared after the traces dry (Figure 2c). The resistance drops as the volume of ink used increases. The resistance drop at low ink volume is mainly explained by the percolation theory, which says that for nanotube and nanowire type materials to form a conductive 2D thin film, the nanotubes/nanowires must form a connected network[23,24]. When the volume of CNT ink used is still low, a continuous connected network of CNT has not formed yet across the whole electrode area and the reduction in electrode resistance with more ink is mainly ascribed to the gradual buildup of such a percolated network. With high ink volume, the deposited CNTs are more than enough to form a percolated network. Hence, the resistance drop is mainly due to increase of electrode thickness (t), following the Ohm's law $R_{CNT} = \rho_{CNT} Wt/l$, where W is the width of the electrode and l is the length of the electrode. After nitric acid treatment, the resistance of the electrode traces all drop compared with untreated ones. The full range XPS of printed SW-CNT with/without acid treatment are compared in Figure 2d, with the XPS of raw SW-CNT added as a reference. The high sodium (Na) contents in the SW-CNT without acid treatment comes from the Na of the SDS surfactant used for preparing the SW-CNT printing ink. More importantly, after acid treatment, no sodium (Na) Auger (~495 eV) signal is detected, which suggests the significant removal of the SDS surfactant. Removing the highly-insulating SDS surfactant improves the electrical contact of nearby nanotube bundles and reduces the overall electrical

resistance of SW-CNT electrodes.[25] High resolution XPS of the C1s, O1s and N1s of the raw SW-CNT and the printed SW-CNT electrode with and without acid treatment are shown in Figure S3-5. Compared with the C1s of the raw SW-CNT and the as-printed SW-CNT without acid treatment, there is a 0.3eV upshift of the C1s binding energy after acid treatment, indicating the oxidation of SW-CNT electrode by the nitric acid.[26] The O1s peak (531.2 eV) in as-printed SW-CNT electrode without acid treatment is attributed to the oxygen from the sulfate (SO_4^-) groups in the SDS surfactant.[27] In acid-treated samples, the O1s peak is shifted to 534.2 eV, which is attributed to the oxidation of SW-CNT by nitric acid.[28] The N1s peak (399.1 eV) in as-printed electrode without acid treatment is attributed to C-N bonding with pyridinic N, and the N1s peak (401.7 eV) in acid-treated sample is attributed to C-N bonding with quaternary N.[29] In summary, the XPS analysis confirms the two effects of acid treatment on the as-printed SW-CNT: (1) it significantly removes the SDS surfactant, which is the main reason for the reduced electrical resistance of the SW-CNT electrode after acid treatment; and (2) it partially oxidizes the SW-CNT, which can improve the contact between SW-CNT electrode and PVA hydrogel electrolyte [30,31].

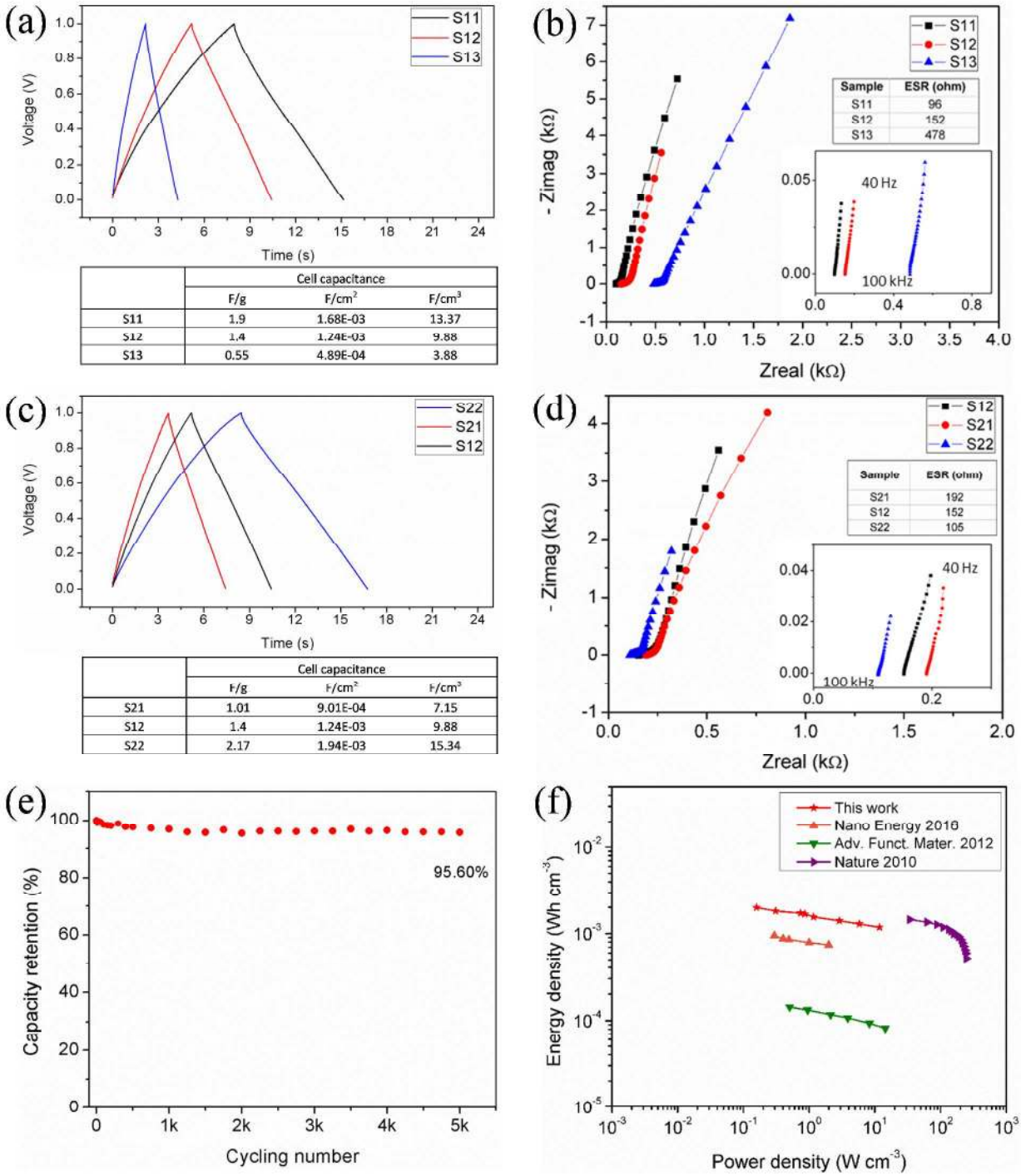

	Cell capacitance		
	F/g	F/cm²	F/cm³
S11	1.9	1.68E-03	13.37
S12	1.4	1.24E-03	9.88
S13	0.55	4.89E-04	3.88

	Cell capacitance		
	F/g	F/cm²	F/cm³
S21	1.01	9.01E-04	7.15
S12	1.4	1.24E-03	9.88
S22	2.17	1.94E-03	15.34

Figure 3. (a) Galvanostatic charge/discharge at 1.32 A cm^{-3} for cells in Study 1 and calculated specific capacitance and cell capacitance. (b) Nyquist plot of Study 1 supercapacitors from potentiostat EIS with inserted zoom-in at high frequency range and table of ESR values. (c)

Galvanostatic charge/discharge at 1.32 A cm^{-3} for cells Study 2 and calculated specific capacitance and cell capacitance. (d) Nyquist plot of Study 2 supercapacitors from potentiostat EIS with inserted zoom-in at high frequency range and table of ESR values. (e) 5000 cycles GCD of cell S22 at 1.32 A cm^{-3}. (f) Ragone plot of cell S22 compared with recent relevant work.

Table 1. Geometries used in electrode and electrolyte design studies.

Geometries*	Study 1			Study 2		
	S11	S12	S13	S21	S12	S22
Width or W (cm)	0.2			0.15	0.2	0.25
Length or L (cm)	2			2		
Gap Distance or D (cm)	0.1	0.2	0.4	0.2		

*Refer to Scheme 1a for how width (W), length (L) and gap distance (D) are defined.

Two studies on how electrode and electrolyte pattern design of the supercapacitor affect its electrochemical performance have been carried out. In the first study, we study the effect of the gap distance between two electrodes ("*D*" in Scheme 1(a)). Three fully-packaged supercapacitors with the same electrode geometry (i.e. width and height) are printed but with different gap distances at 1 mm, 2 mm, and 4 mm, thereafter referred as S11, S12, and S13 respectively. The exact geometry of the cells can be found in Table 1. The volume of SW-CNT ink is adjusted so that the density and thickness of SW-CNT is kept the same for S11, S12, and S13. To evaluate the electrochemical performance of the printed supercapacitors, galvanostatic charge-discharge (GCD), potentiostat EIS and cyclic voltammetry (CV) are performed at different conditions. The GCD curves of S11-S13 between 0-1 V at a current density of 1.32 A cm^{-3} and the calculated specific capacitance are shown in Figure 3a. All GCD curves have symmetric charge and discharge profiles, however it is obvious that S11 with the smallest electrode-gap distance of 1

mm has the highest specific capacitance of 13.37 F cm^{-3} (1.9F g^{-1} and 1.68 mF cm^{-2}) followed by S12 and S13. There is a clear decreasing trend for the specific capacitance as the electrode-gap distance increases. The reason for this observed trend could be understood from the EIS of the three supercapacitors (Figure 3b). The Nyquist plots are almost-vertical straight lines at low frequencies, characteristic of capacitive behaviors.[32–34] Intersect of the Nyquist plot with the real axis at high frequency is the equivalent series resistance (ESR) of the supercapacitor, which consists of resistances from both the electrode and electrolyte. Large ESR will cause large drop of voltage at the beginning of discharge, which decreases the usable discharge voltage window and capacity of the supercapacitor. As shown in Figure 3b, as the electrode-gap distance is increasing, the ESR increases from 95 ohms for S11 to 478 ohms for S13, mainly caused by the increased electrolyte resistance since the electrodes in all three cells are identical. The larger electrolyte resistance in S13 is caused by the larger electrode gap as explained in Table S1 and associated discussion in the Supporting Information. In short, for planar supercapacitors the electrolyte resistance (R_s) can be expressed as $R_s = \rho\kappa$, where ρ is the resistivity of the electrolyte and κ is the cell constant. As the gap distance increases, the cell constant also increases leading to higher electrolyte resistance R_s and degraded capacitive performance.[35] From this study, it can be concluded that reducing the electrode-gap distance can enhance the capacitance of the as-printed supercapacitor. However, the printing resolution of DIW with the developed CNT ink limits how small the gap distance can be. Printing extra small gap distance beyond the resolution of DIW may lead to partial overlapping of two adjacent electrodes and the shorting of the two electrodes, which results in a completely malfunctioned device.

In the second study, the electrode-gap distance ("*D*" in Scheme 1a) and the height of the electrode pattern ("*L*" in Scheme 1a) are kept the same but the width of the electrode pattern

("*W*" in Scheme 1a) is changed from 1.5 mm to 2 mm and 2.5 mm, thereafter denoted as S21, S12, S22 respectively. The exact geometry of the cells can be found in Table 1. The volume of SW-CNT ink is adjusted so that the density and thickness of SW-CNT is kept the same for S21, S12, and S22. Specifically, the GCD curves of S21, S12, S22 between 0-1 V at a current density of 1.32 A cm^{-3} and the calculated specific capacitance are shown in Figure 3c. It is found that the specific capacitance increases as the electrode width increases from S21 (7.15 F cm^{-3}) to S22 (15.34 F cm^{-3}). The Nyquist plots in Figure 3d show that the ESR decreases as the electrode width increases. Different from study 1, this change in ESR in study 2 is caused by the changes of both the electrode resistance and the electrolyte resistance as the electrode width changes. Obviously, wider electrode patterns can lower the electrode resistance and enhance the capacitance of the printed supercapacitors. In addition, increasing electrode width also leads to the decrease of electrolyte resistance for planar supercapacitors,[35] according to the analysis presented in Table S1 and the associated discussion in the Supporting Information. It should be noted that for optimal supercapacitor performance, the electrode width should not be arbitrarily large. As shown in the simulated electric field near the planar electrodes in Figure S6, the electric field becomes weaker at locations away from the edge of the electrodes, and so as the electrostatic force driving the formation of electric double layers (EDL). Thus, the active materials away from the electrode edges do not contribute as much EDL capacitance as those near the edges and the overall specific capacitance is decreased. With relatively narrow width, the benefits of increasing electrode width (i.e. lower electrode and electrolyte resistance) will overshadow the effect of non-uniform electric field and the specific capacitance will increase with electrode width (as shown in our study 2 results). It is expected that with extra wide electrode, the effect of non-uniform electric field will eventually become more significant than

the benefits of wide electrode and the specific capacitance will start decreasing with the increase of electrode width.

Table 2. Performance comparison of Carbon based planar supercapacitor

Active material	Electrolyte	Technique	capacitance	Energy density	Power density	Year	Ref.
Graphene	LiCl/PVA	laser process	0.694 F cm^{-3}	0.98 mWh cm^{-3}	0.3 W cm^{-3}	2016	[19]
carbon onion	Et_4NBF_4/anhydrous propylene carbonate	Laser process	1.3 F cm^{-3}	1.5 mWh cm^{-3}	35 W cm^{-3}	2010	[36]
Graphene	H_3PO_4/PVA	Inkjet printing	99 μ F cm^{-2}	N/A	N/A	2017	[37]
Reduced Graphene	H_2SO_4/PVA	MEMS	17.9 F cm^{-3}	2.5 mWh cm^{-3}	495 W cm^{-3}	2013	[32]
CNT	KCl	MEMS	6.1 F cm^{-3}	0.15 mWh cm^{-3}	0.3 W cm^{-3}	2012	[38]
Carbonized polyimide	H_2SO_4/PVA	laser process	42.6 mF cm^{-2}	N/A	N/A	2017	[39]
Carbon nanotube	LiCl/PVA	DIW	15.34 F cm^{-3}	1.2 mWh cm^{-3}	11.8 W cm^{-3}	2017	This Work

Cell S22 with the highest specific capacitance is used for further studies. Cyclic stability study (Figure 3e) showed that S22 can maintain ~96.5% of its initial capacitance after 5000 cycles of GCD at 1.32 A cm^{-3}. The energy density and power density of cell S22 are calculated using equation (5) and (6) at varied current density from 0.02 A cm^{-3} to 20 A cm^{-3} and compared with recent planar carbon based electric double layer capacitors (EDLCs) on Figure 3f. The S22 cell has a high energy density of 1.18 mWh cm^{-3} at power density of 11.8 W cm^{-3}. The energy and power performance of the as-printed fully-packaged supercapacitor is among the best in recently reported planar electric double layer capacitors and even higher than some graphene based

supercapacitors (Table 2), which involved high cost fabrication process such as lithography patterning and high temperature annealing.

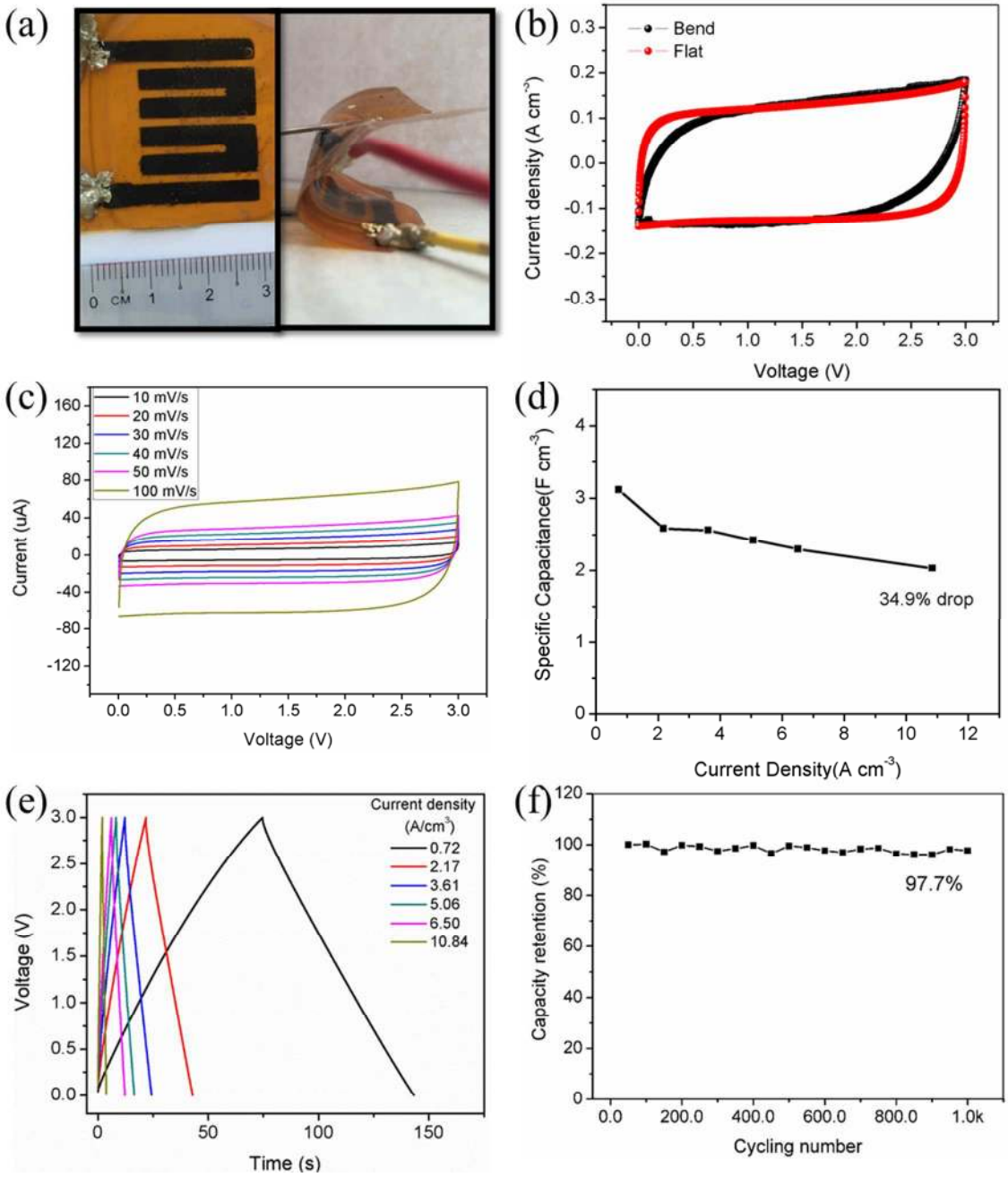

Figure 4. (a) Optical picture of the as-printed 3-cell supercapacitor array; 160° bended supercapacitor array; (b) CV comparison of bent and flat cells; (c) CV profiles of 3-cell supercapacitor at different scan rates; (d) Calculated specific capacitance at different current

density; (e) Galvanostatic charge/discharge of 3-cell supercapacitor at varied current densities; (f) Cyclic performance of 3-cell supercapacitor at a constant 5.06 A cm^{-3} current density GCD.

An array of three supercapacitors connected in series is printed. Picture of the printed supercapacitor array is shown in Figure 4a. The SW-CNT electrode can be clearly seen in the picture, whereas the transparent electrolyte and silicone seal cannot be discerned in the picture. The supercapacitor is connected to electrical wires by silver paste. Since all components including the electrodes, the electrolyte, the substrate, and the seal are flexible, the as-printed supercapacitor showed excellent flexibility. CV test is performed when the cell is bent and the bent cell retains similar performance compare to unbent flat cell (Figure 4b), which proves the mechanical flexibility of the cell.

A series of CV tests is performed with a potential window of 0-3 V and varied scan rates of 10, 20, 30, 40, 50, and 100 mV s^{-1}. The CV curves (Figure 4c) all have rectangle shapes, which confirms the printed device is a pure electric double layer capacitor. The GCD curves measured at current densities 0.72, 2.17, 3.61, 5.06, 6.50, 10.84 A cm^{-3} are shown in Figure 4e. The charge and discharge curves are highly symmetric. Specific capacitances of the supercapacitor array are calculated by equation (1) and plotted at different current densities (Figure 4d). The specific capacitance only drops by 34.9 % when current density increases from 0.72 A cm^{-3} to 10.84 A cm^{-3} demonstrating good rate capability.

The cyclic stability is investigated by performing GCD at a current density of 5.06 A cm^{-3} (Figure 4f). There is no significant decrease of cell capacitance (~2.42 F cm^{-3}) and the capacitance is retained 97.7 % after 1000 cycles of charge/discharge. It is noted that the capacitance increases after a few cycles at the beginning of the cyclic test. This increase can be

attributed to the increase of SW-CNT surface area induced by the surface activation effect of the charge/discharge process.

3. Conclusion

In this study, we report for the first time the direct ink writing (DIW) of fully-packaged supercapacitors on flexible polymer substrate. Different supercapacitor designs have been implemented by the DIW and electrochemical study results show that smaller gap spacing between two electrodes and wider electrode facilitate the fast ion transport and electron transport respectively, which improve the overall cell performance. A multi-cell supercapacitor array with three identical cells connected in series is printed to demonstrate the scalability of the developed technology. The direct-written fully-packaged SW-CNT supercapacitor has comparable energy and power performances to recently reported planer carbon-based supercapacitors fabricated by other printing or non-printing methods. The developed ink formula and direct ink writing setup enable the mask-free, transfer-free, and alignment-free printing with precise and repeatable control on the spatial distribution of different functional materials. It paves the way for rapid, low cost, and scalable manufacturing of high performance fully-packaged supercapacitors for practical applications.

(1) Homenick, C. M.; James, R.; Lopinski, G. P.; Dunford, J.; Sun, J.; Park, H.; Jung, Y.; Cho, G.; Malenfant, P. R. L. Fully Printed and Encapsulated SWCNT-Based Thin Film Transistors via a Combination of R2R Gravure and Inkjet Printing. *ACS Appl. Mater. Interfaces* **2016**, *8*, 27900–27910.

(2) Medina-Sánchez, M.; Martínez-Domingo, C.; Ramon, E.; Merkoçi, A. An Inkjet-Printed Field-Effect Transistor for Label-Free Biosensing. *Adv. Funct. Mater.* **2014**, *24*, 6291–

6302.

(3) Kulkarni, M. V; Apte, S. K.; Naik, S. D.; Ambekar, J. D.; Kale, B. B. Ink-Jet Printed Conducting Polyaniline Based Flexible Humidity Sensor. *Sensors Actuators B Chem.* **2013**, *178*, 140–143.

(4) Lindh, E. M.; Sandström, A.; Edman, L. Inkjet Printed Bilayer Light-Emitting Electrochemical Cells for Display and Lighting Applications. *Small* **2014**, *10*, 4148–4153.

(5) Zhou, N.; Liu, C.; Lewis, J. A.; Ham, D. Gigahertz Electromagnetic Structures via Direct Ink Writing for Radio-Frequency Oscillator and Transmitter Applications. *Adv. Mater.* **2017**, *29*, 1605198--n/a.

(6) Malone, E.; Rasa, K.; Cohen, D.; Isaacson, T.; Lashley, H.; Lipson, H. Freeform Fabrication of Zinc-Air Batteries and Electromechanical Assemblies. *Rapid Prototyp. J.* **2004**, *10*, 58–69.

(7) Kim, Y. H.; Yoo, B.; Anthony, J. E.; Park, S. K. Controlled Deposition of a High-Performance Small-Molecule Organic Single-Crystal Transistor Array by Direct Ink-Jet Printing. *Adv. Mater.* **2012**, *24*, 497–502.

(8) Liu, Y.; Cui, T.; Varahramyan, K. All-Polymer Capacitor Fabricated with Inkjet Printing Technique. *Solid. State. Electron.* **2003**, *47*, 1543–1548.

(9) Liu, N.; Zhou, Y.; Ai, N.; Luo, C.; Peng, J.; Wang, J.; Pei, J.; Cao, Y. High-Performance, All-Solution-Processed Organic Nanowire Transistor Arrays with Inkjet-Printing Patterned Electrodes. *Langmuir* **2011**, *27*, 14710–14715.

(10) Sirringhaus, H.; Kawase, T.; Friend, R. H.; Shimoda, T.; Inbasekaran, M.; Wu, W.; Woo,

E. P. High-Resolution Inkjet Printing of All-Polymer Transistor Circuits. *Science (80-.).* **2000**, *290*, 2123–2126.

(11) Maynor, B. W.; Filocamo, S. F.; Grinstaff, M. W.; Liu, J. Direct-Writing of Polymer Nanostructures: Poly(thiophene) Nanowires on Semiconducting and Insulating Surfaces. *J. Am. Chem. Soc.* **2002**, *124*, 522–523.

(12) Muth, J. T.; Vogt, D. M.; Truby, R. L.; Meng????, Y.; Kolesky, D. B.; Wood, R. J.; Lewis, J. A. Embedded 3D Printing of Strain Sensors within Highly Stretchable Elastomers. *Adv. Mater.* **2014**, *26*, 6307–6312.

(13) Boley, J. W.; White, E. L.; Chiu, G. T. C.; Kramer, R. K. Direct Writing of Gallium-Indium Alloy for Stretchable Electronics. *Adv. Funct. Mater.* **2014**, *24*, 3501–3507.

(14) Wehner, M.; Truby, R. L.; Fitzgerald, D. J.; Mosadegh, B.; Whitesides, G. M.; Lewis, J. A.; Wood, R. J. An Integrated Design and Fabrication Strategy for Entirely Soft, Autonomous Robots. *Nature* **2016**, *536*, 451–455.

(15) Lewis, J. A. Direct Ink Writing of 3D Functional Materials. *Adv. Funct. Mater.* **2006**, *16*, 2193–2204.

(16) Lewis, J. A.; Smay, J. E.; Stuecker, J.; Cesarano, J. Direct Ink Writing of Three-Dimensional Ceramic Structures. *J. Am. Ceram. Soc.* **2006**, *89*, 3599–3609.

(17) Li, R.-Z.; Hu, A.; Zhang, T.; Oakes, K. D. Direct Writing on Paper of Foldable Capacitive Touch Pads with Silver Nanowire Inks. *ACS Appl. Mater. Interfaces* **2014**, *6*, 21721–21729.

(18) Wei, H.; Zhang, Q.; Yao, Y.; Liu, L.; Liu, Y.; Leng, J. Direct-Write Fabrication of 4D

Active Shape-Changing Structures Based on a Shape Memory Polymer and Its Nanocomposite. *ACS Appl. Mater. Interfaces* **2017**, *9*, 876–883.

(19) Xie, B.; Wang, Y.; Lai, W.; Lin, W.; Lin, Z.; Zhang, Z.; Zou, P.; Xu, Y.; Zhou, S.; Yang, C.; *et al.* Laser-Processed Graphene Based Micro-Supercapacitors for Ultrathin, Rollable, Compact and Designable Energy Storage Components. *Nano Energy* **2016**, *26*, 276–285.

(20) Wang, S.; Liu, N.; Tao, J.; Yang, C.; Liu, W.; Shi, Y.; Wang, Y.; Su, J.; Li, L.; Gao, Y. Inkjet Printing of Conductive Patterns and Supercapacitors Using a Multi-Walled Carbon nanotube/Ag Nanoparticle Based Ink. *J. Mater. Chem. A* **2015**, *3*, 2407–2413.

(21) Tehrani, Z.; Thomas, D. J.; Korochkina, T.; Phillips, C. O.; Lupo, D.; Lehtimäki, S.; O'Mahony, J.; Gethin, D. T. Large-Area Printed Supercapacitor Technology for Low-Cost Domestic Green Energy Storage. *Energy* **2017**, *118*, 1313–1321.

(22) Gogotsi, Y.; Simon, P. True Performance Metrics in Electrochemical Energy Storage. *Science (80-.).* **2011**, *334*, 917–918.

(23) Hu, L.; Hecht, D. S.; Grüner, G. Percolation in Transparent and Conducting Carbon Nanotube Networks. *Nano Lett.* **2004**, *4*, 2513–2517.

(24) Pike, G. E.; Seager, C. H. Percolation and Conductivity: A Computer Study. I. *Phys. Rev. B* **1974**, *10*, 1421–1434.

(25) Geng, H.-Z.; Kang, K.; Kang, K.; So, P.; Lee, Y. S.; Chang, Y.; Lee, Y. H. Effect of Acid Treatment on Carbon Nanotube-Based Flexible Transparent Conducting Films.

(26) Kwon, J.-Y.; Kim, H.-D. Preparation and Properties of Acid-Treated Multiwalled Carbon Nanotube/waterborne Polyurethane Nanocomposites. *J. Appl. Polym. Sci.* **2005**, *96*, 595–

604.

(27) Terlingen, J. G. A.; Feijen, J.; Hoffman, A. S. Immobilization of Surface Active Compounds on Polymer Supports Using Glow Discharge Processes. *J. Colloid Interface Sci.* **1993**, *155*, 55–65.

(28) Xie, Y.; Sherwood, P. M. A. E□35 Pitch□based Carbon Fiber by Core Level and Valence Band XPS. *Surf. Sci. Spectra* **1992**, *1*, 198–203.

(29) Daems, N.; Sheng, X.; Vankelecom, I. F. J.; Pescarmona, P. P. Metal-Free Doped Carbon Materials as Electrocatalysts for the Oxygen Reduction Reaction. *J. Mater. Chem. A* **2014**, *2*, 4085–4110.

(30) Tang, X.; Lui, Y. H.; Chen, B.; Hu, S. Functionalized Carbon Nanotube Based Hybrid Electrochemical Capacitors Using Neutral Bromide Redox-Active Electrolyte for Enhancing Energy Density. *J. Power Sources* **2017**, *352*, 118–126.

(31) Jin, H.; Wang, X.; Gu, Z.; Polin, J. Carbon Materials from High Ash Biochar for Supercapacitor and Improvement of Capacitance with HNO3 Surface Oxidation. *J. Power Sources* **2013**, *236*, 285–292.

(32) Wu, Z.; Parvez, K.; Feng, X.; Müllen, K. Graphene-Based in-Plane Micro-Supercapacitors with High Power and Energy Densities. *Nat. Commun.* **2013**, *4*.

(33) Sheng, K.; Sun, Y.; Li, C.; Yuan, W.; Shi, G. Ultrahigh-Rate Supercapacitors Based on Eletrochemically Reduced Graphene Oxide for Ac Line-Filtering. *Sci. Rep.* **2012**, *2*.

(34) Kötz, R.; Carlen, M. Principles and Applications of Electrochemical Capacitors. *Electrochim. Acta* **2000**, *45*, 2483–2498.

(35) Olthuis, W.; Streekstra, W.; Bergveld, P. Theoretical and Experimental Determination of Cell Constants of Planar-Interdigitated Electrolyte Conductivity Sensors. *Sensors Actuators B. Chem.* **1995**, *24*, 252–256.

(36) Pech, D.; Brunet, M.; Durou, H.; Huang, P.; Mochalin, V.; Gogotsi, Y.; Taberna, P.-L.; Simon, P. Ultrahigh-Power Micrometre-Sized Supercapacitors Based on Onion-like Carbon. *Nat. Nanotechnol.* **2010**, *5*, 651–654.

(37) Sollami Delekta, S.; Smith, A. D.; Li, J.; Ostling, M. Inkjet Printed Highly Transparent and Flexible Graphene Micro-Supercapacitors. *Nanoscale* **2017**, *9*, 6998–7005.

(38) Beidaghi, M.; Wang, C. Micro-Supercapacitors Based on Interdigital Electrodes of Reduced Graphene Oxide and Carbon Nanotube Composites with Ultrahigh Power Handling Performance. *Adv. Funct. Mater.* **2012**, *22*, 4501–4510.

(39) Wang, S.; Yu, Y.; Li, R.; Feng, G.; Wu, Z.; Compagnini, G.; Gulino, A.; Feng, Z.; Hu, A. High-Performance Stacked in-Plane Supercapacitors and Supercapacitor Array Fabricated by Femtosecond Laser 3D Direct Writing on Polyimide Sheets. *Electrochim. Acta* **2017**, *241*, 153–161.

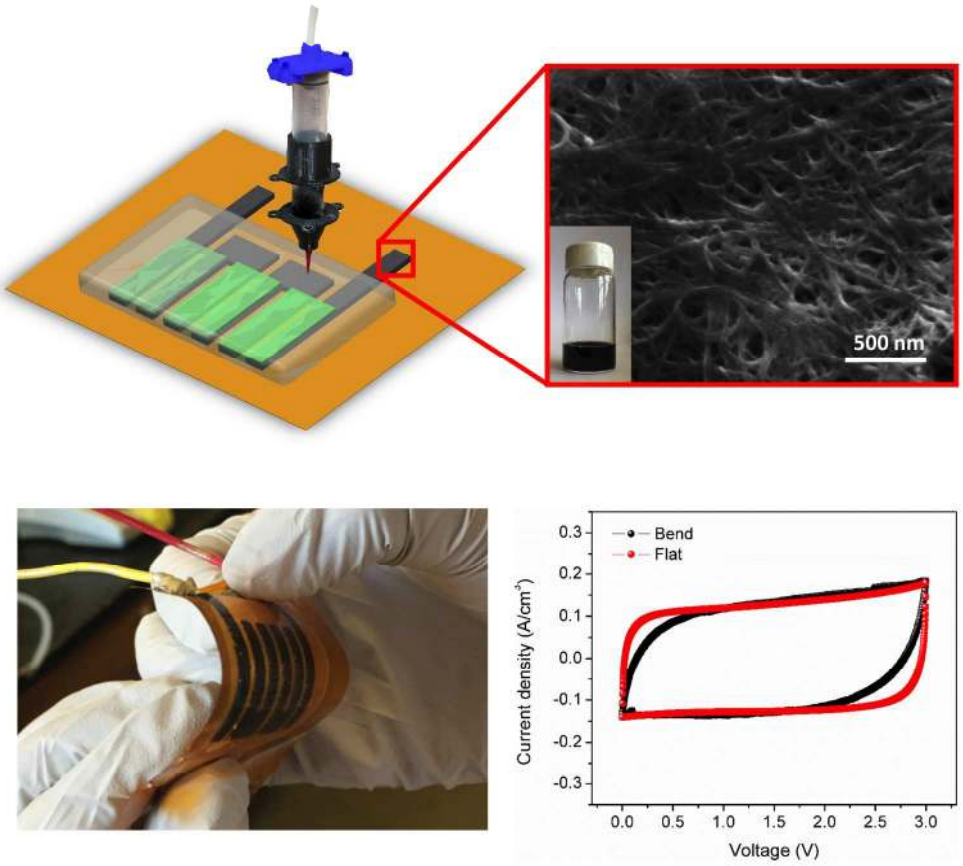

Table of Contents (TOC) Graphic

215x223mm (300 x 300 DPI)